PHYSICAL REVIEW E VOLUME 53, NUMBER 6 JUNE 1996

Homoclinic dynamics in experimental Shil'nikov attractors

R. Herrero, R. Pons, J. Farjas, F. Pi, and G. Orriols
Departament de Física, Universitat Autònoma de Barcelona, 08193 Bellaterra, Spain

(Received 30 November 1995)

We report the experimental observation of Shil'nikov-type attractors in the reflection of optothermal nonlinear devices, evidencing homoclinic phenomena associated with a variety of saddle set configurations. Recurrent phase-space operations underlying the homoclinic dynamics are evidenced by analysis of proper Poincaré sections. In the case of a saddle limit cycle, deterministic aperiodic evolutions are pointed out clearly by means of high-order multibranched first-return maps. [S1063-651X(96)01106-3]

PACS number(s): 05.45.+b, 42.65.Pc

I. INTRODUCTION

In recent years the crucial role played by homoclinic orbits in the mechanisms originating chaos in dynamical systems has become apparent [1,2]. Homoclinic orbits are trajectories biasymptotic to a saddle limit set both forward and backward in time. The homoclinic orbit characterizes a recurrent mechanism for global folding of the phase space, while the saddle set provides stretching, folding, and contraction of the flow at a local level. According to the actual saddle configuration, chaos may appear when a parameter is varied towards the homoclinicity condition.

The simplest and most clear situation yielding homoclinic chaos in dissipative systems is associated with the so-called Shil'nikov-type attractors. Such attractors usually arise in three-dimensional phase spaces from a growing periodic orbit that approaches an external saddle set to become homoclinic to it. The saddle may be either an inward spiraling focus or a limit cycle of diameter lower than the homoclinic orbit radius. In cases of larger saddle cycles, the attractor evolves in a different way, yielding the so-called Rössler-type attractors. The bending of the orbit is so large in these cases that it may be reinjected close to the inner fixed point from which it was originated. After the Hopf bifurcation this point has become an outward spiraling saddle focus and thus the attractor evolution may involve homoclinicities of two kinds associated with either the internal or the external saddle set and heteroclinic connections between them [3,4]. In any case a theorem by Shil'nikov [5] proves that complex dynamics will occur near homoclinicity when an inequality is satisfied between the eigenvalues of the linearized flow around the saddle point, i.e., if the real eigenvalue is larger in modulus than the real part of the complex eigenvalue. Complex behavior always occurs when the saddle set is a limit cycle [6].

Attractor structures and bifurcation sequences in homoclinic transitions have been investigated by means of two-dimensional Poincaré maps constructed by considering the linear evolution near the saddle and a nonlinear reinjection mechanism associated with the homoclinic connection [4,7–10]. Such a kind of construction yields one-dimensional first-return maps in the strong area contraction limit, which consist of either multiple humps or multiple branches accumulating towards the homoclinicity point and which constitute a clear signature of the homoclinic bifurcation. Map analysis points out a rather complex process that may involve accumulated cascades of periodic windows bounded by tangent bifurcations and period-doubling sequences, the creation of successive horseshoes, the occurrence of a variety of subsidiary homoclinic connections, and other more subtle phenomena [1,2]. The process appears to be extremely sensitive to the control parameter. The problem becomes more critical as the saddle becomes closer to the Shil'nikov condition because the interval of the control parameter leading to complex behavior then becomes narrower and closer to the homoclinicity point.

On the other hand, the evolution of Rössler-type attractors involves homoclinicities of two different saddle sets and heteroclinic connections between them. The process usually covers a large interval of the control parameter and the observation of aperiodic behaviors appears to be easier than in the Shil'nikov-type case. As a matter of fact, experimental observation of multiple-structure return maps has been reported in the Belousov-Zhabotinskii reaction [11], in a laser with feedback [12], in a laser with a saturable absorber [13–15], in the plasma of a glow discharge [16], and in an optically bistable device like the one here considered [17]. Homoclinic chaos has been also evidenced in a modified Van der Pol electrical oscillator [18], in a catalytic oxidation of methanol [19], and during copper electrodissolution [20]. In most of these experiments homoclinicity appears associated with an outward spiraling saddle set and the observed phase portraits are in the form of folded bands. Only the experiment on a laser with feedback by Arecchi *et al.* [12] corresponds to an inward spiraling saddle focus even if, in this case, the trajectory visits the neighborhoods of other two saddle points.

In this paper we report the experimental observation of Shil'nikov-type attractors in the response of an optothermal nonlinear device irradiated by a laser beam, evidencing homoclinic phenomena associated with a variety of saddle set configurations, i.e., focus points either fulfilling or not the Shil'nikov condition and limit cycles generated by Hopf bifurcation of the saddle point. Particular emphasis is given to the case of a saddle point fulfilling closely the Shil'nikov condition and providing really clear phase portrait structures of the Shil'nikov type. The recurrent phase-space operations underlying the homoclinic dynamics are pointed out by analysis of proper Poincaré sections and a two-stage return map is used to show how critical the noise influence on the deterministic evolution is. Good agreement is found with predictions of a Poincaré map model [9]. In the case of homoclinicity to a saddle limit cycle, deterministic aperiodic evolutions are pointed out clearly by means of high-order multibranched first-return maps.

II. OPTOTHERMAL NONLINEAR DEVICE

The nonlinear device is based on the so-called optothermal bistability with localized absorption (BOITAL) [21] and consists of a Fabry-Pérot cavity where the input mirror is a partially absorbing film, the rear mirror is a high-reflection dielectric coating, and the spacer between mirrors is a multilayer of transparent materials having alternatively opposite thermo-optic effects. When illuminated by a light beam, the interferometer response is affected by a nonlinear feedback loop involving (i) light absorption in the input mirror film and the consequent heat propagation from the localized source through the cavity spacer, (ii) temperature effects on the cavity optical length by thermal expansion and refractive index variation, and (iii) light interference effects where absorption takes place. Nonlinearity is exclusively contained in the function $A(\psi)$ describing the interferometer absorption as a function of the round-trip phase shift ψ and related to the Airy function of the interferometer. The device nonlinearity enhances with the interferometer absorption contrast, which requires proper design of the input reflective film, and with spacer parameters determining the feedback loop efficiency, i.e., thicknesses, thermal and thermo-optic coefficients of the multilayer materials [21].

The nonlinear feedback is responsible for the multistable stationary response of BOITAL étalons and, in the case of multilayer spacers, is affected by the competing phase-shift contributions of the various layers. The relative position of the layers with respect to the localized heat source introduces time delays between such contributions and, in this way, it is possible to have sustained oscillations and other sorts of instabilities in the response of the system. Thus time dynamics in multilayer BOITAL devices is exclusively based on heat propagation from the absorbing mirror through the cavity spacer, while light provides an instantaneous nonlinear feedback by testing the spacer temperature through its own phase shift and transferring such information to the localized heat source by means of interference effects.

Under some simplifying assumptions, the BOITAL cavity with a multilayer space may be described by a set of homogeneous heat equations subject to the proper continuity and boundary conditions, of which the one describing the localized heat source is nonlocal and nonlinear [22]. The stationary solution of this partial differential equation (PDE) system as a function of the incident intensity yields a multivalued branching diagram with features depending on the interferometric function, but not on the multilayer structure. The spacer parameters affect the stationary branching diagram through a scale factor only. The linear-stability analysis point out that the effective dimension of the dynamical problem may be considered equal to N, the number of layers into the cavity spacer, and that the system may experience up to N-1 Hopf bifurcations [22]. Extensive numerical simulations for N up to 3 allowed us to verify the linear-stability conclusions and to deduce that a suitable basis for the reduced phase space is the one defined by the partial phase shifts associated with the various layers [22]. We have also shown that the PDE system may be reduced to a Nth-order model of ordinary differential equations (ODEs) that involves the partial phase shifts as variables and exhibits local and global dynamics very similar to the ones of the original system [23].

A comment is worthwhile concerning materials exhibiting phase-shifts effects with different inertia with respect to thermal excitation [24]. In most materials, mechanical expansion and refractive index variation take place simultaneously and their light phase-shift effects are characterized by the single coefficient resulting from the addition (or subtraction) of partial coefficients. But this is not the case for some composite materials in which mechanical expansion seems to work slower than refractive index variations. Such a kind of material introduces two time-delayed phase-shift effects that, on the other hand, may be competing since usually such materials have a negative thermo-optic effect. As a consequence, layers of these materials introduce additional degrees of freedom within the BOITAL cavity and effective dimensions higher than N may be obtained with N-layer spacers. It is really useful from the experimental point of view because the lower the number of layers the easier the device manipulation. On the other hand, the ODE model may be easily extended to describe BOITAL systems containing such materials. In that case the given layer is described by two partial phase shifts, each one subject to the same dynamic equation but with proper adjustments on the relaxation time constant and thermo-optic coefficient.

The BOITAL systems exhibit a rich variety of homoclinic phenomena. In the case of bidimensional devices, the occurrence of oscillations through a Hopf instability and a variety of homoclinic bifurcations without complicated orbit structure have been observed both numerically and experimentally [25]. This paper deals with tridimensional systems and the experimental results show the occurrence of Shil'nikov-type attractors associated with a variety of saddle sets. In a previous paper we have shown that the same kind of device may originate folded chaotic bands of the Rössler type [17]. In fact, both experiments and numerical simulations point out clearly strong similarities between the dynamics exhibited by the third-order system, currently known as the Rössler model [26], and by the tridimensional BOITAL systems when a unique pair of saddle-node points are involved. The mathematical origin of such similarities has been evidenced by comparing canonical forms of both the BOITAL third-order ODEs and Rössler models [23].

III. ELEMENTS OF A POINCARÉ MAP MODEL

A useful tool for analysis of homoclinic bifurcations is provided by Poincaré maps constructed by decomposing the dynamics into two distinct stages, i.e., the linear evolution near the saddle characterized by the corresponding eigenvalues λ and $\rho \pm i\omega$, and a nonlinear reinjection mechanism associated with the homoclinic connection [4,7,8]. Such a kind of Poincaré map has been generalized recently to permit the simultaneous description of homoclinic tangencies to either a point or a periodic orbit [9,10]. We introduce here some elements of this map for the case of a focus point because they will be used in the analysis of experimental

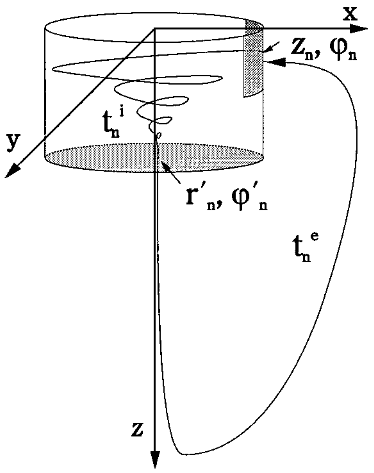

FIG. 1. Schematic representation of the Poincaré map model used to characterize the homoclinic bifurcation associated with an inward spiraling saddle focus.

results. Using cylindrical coordinates centered on the point and considering the scheme outlined in Fig. 1 [9], we define the first stage as $F(r=1,\varphi_n,z_n)=(r'_n,\varphi'_n,z=1)$, with

$$r'_n=\exp(\rho t^i_n), \tag{1a}$$

$$\varphi'_n=\varphi_n+\omega t^i_n, \tag{1b}$$

where

$$t^i_n=-\frac{1}{\lambda}\ln z_n \tag{2}$$

represents the flying time within the cylinder. Within the linear region, the saddle stable manifold remains contained in the $z=0$ plane, while the unstable manifold goes along the z axis. According to numerical simulations [22] and experimental attractors, in which strong contraction in a certain direction is evident, the second stage is defined as the map $G(r'_n,\varphi'_n,z=1)=(r=1,\varphi_{n+1},z_{n+1})$, with

$$z_{n+1}=b+fr'_n\cos\varphi'_n\cos\gamma, \tag{3a}$$

$$\varphi_{n+1}=-(z_{n+1}-b)\tan\gamma, \tag{3b}$$

where full contraction along the y axis is assumed, the factor $f<1$ describes a global compression in the section plane, the angle γ describes some rotation of the contracted flow, and b gives the z position at which the unstable manifold impinges on the lateral surface with respect to the stable manifold, i.e., $b=0$ means homoclinicity. The strong contraction limit implies that map G reinjects always in a little straight segment and γ is the angle this segment forms with the z axis. The full contraction implies also that the dynamics may be fully described by one-dimensional maps as the ones obtained in first-return representations of either time returns or phase-space coordinates.

One-dimensional (1D) return maps for the space variables may be easily derived from Eqs. (3), (1), and (2), while additional assumptions concerning the external reinjection time t^e are necessary in order to obtain time return maps. Both experiments and numerical simulations suggest as reasonable to suppose the reinjection time as given by

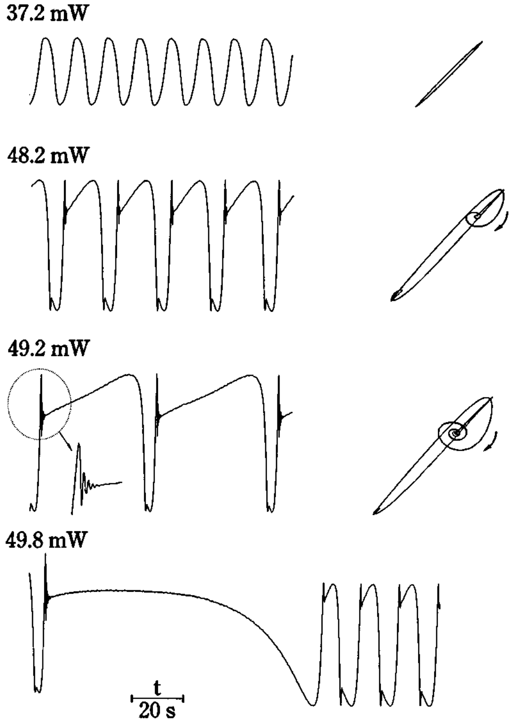

FIG. 2. Time evolution of the reflected power and reconstructed phase portrait for different incident light powers on the glass-silicone-glass system at 22°C. The signal at 49.8 mW includes a transient illustrating the homoclinic transition to a different oscillating state.

$$t^e_n=T^e-\beta(z_{n+1}-b)=T^e-\beta fr'_n\cos\varphi'_n\cos\gamma, \tag{4}$$

where T^e is the reinjection time on the unstable manifold and β is a factor characterizing some time spread in proportion to the z distance between the given trajectory and the unstable manifold. If the external time spread is not significant with respect to the total return time, it is reasonable to assume t^e as a constant [12] and the first-return map may then be characterized by the internal time map derived from Eqs. (2), (3a), and (1) as

$$t^i_{n+1}=-\frac{1}{\lambda}\ln(b+f\exp(\rho t^i_n)\times\cos\{\omega t^i_n-[\exp(-\lambda t^i_n)-b]\tan\gamma\}\cos\gamma). \tag{5}$$

Nevertheless, if significant, the external time spread may be pointed out by analyzing internal orbit correlations as the ones expressed by the two-stage map

$$t^e_n(t^i_n)=T^e-\beta f\exp(\rho t^i_n)\cos\{\omega t^i_n-[\exp(-\lambda t^i_n)-b]\tan\gamma\}\times\cos\gamma, \tag{6a}$$

$$t^i_{n+1}(t^e_n)=-\frac{1}{\lambda}\ln\left(b+\frac{1}{\beta}(T^e-t^e_n)\right), \tag{6b}$$

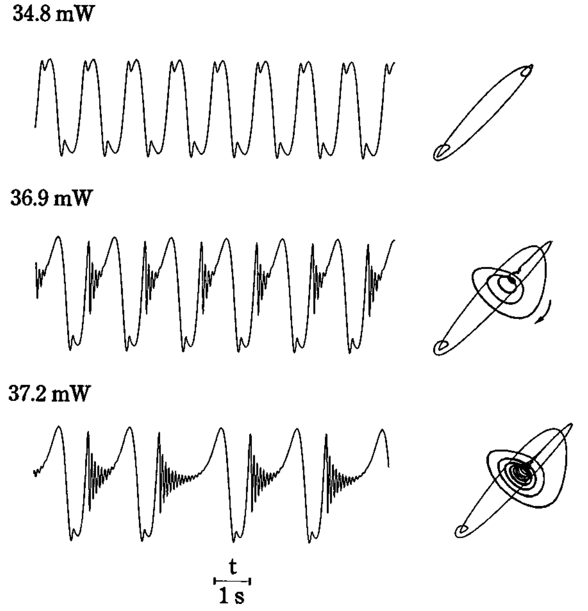

FIG. 3. Time evolution of the reflected power and reconstructed phase portrait for three incident powers on the glass-adhesive system at 25°C.

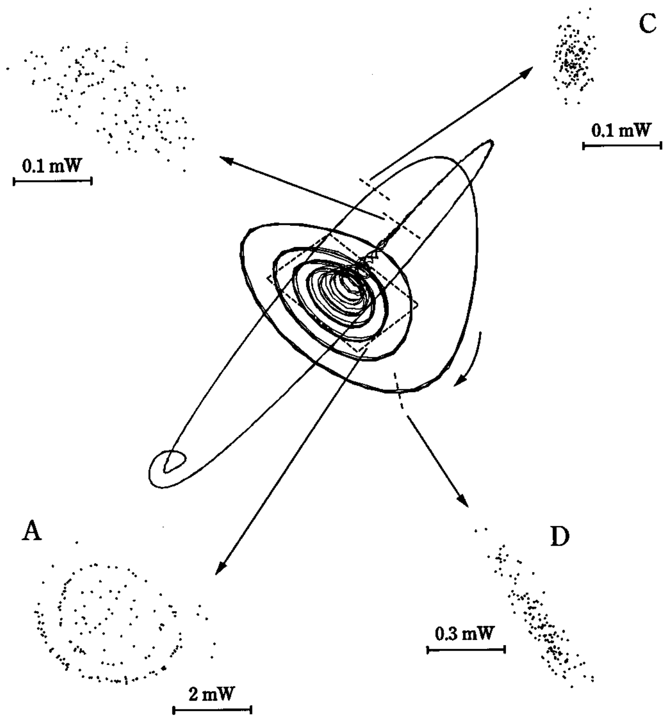

FIG. 4. Four Poincaré sections of the 37.2-mW phase portrait of Fig. 3. Each section contains 138 points while the represented phase portrait includes four orbits only.

where the internal and external times are given by Eqs. (2) and (4), respectively. As it will be shown below, such a kind of two-stage representation is also useful for analyzing noise effects upon the dynamical evolution.

IV. EXPERIMENTAL DETAILS

Experiments were performed with nonlinear devices based on two different spacer structures within the cavity determined by a partially absorbing metal film and a high-reflection dielectric mirror. One device was spaced with a glass–silicone [27] –glass trilayer of thicknesses 400 μm, 250 μm, and 1 mm, respectively, and the other with a glass–optical adhesive [28] bilayer structure of 140 and 590 μm, respectively. In the case of glass, thermal expansion works as a positive effect (10^{-5} K^{-1}), while the silicone and the optical adhesive produce negative phase-shifting effects essentially due to refractive index changes. Relative variations of the optical path with temperature for these materials were estimated to be -4.7×10^{-4} and -3.2×10^{-4} K^{-1} at 22 °C, respectively. No separate estimations for thermal expansion and thermo-optic coefficients were performed. The optical adhesive exhibits thermal expansion and the thermo-optic effect with different time inertia [24] and the glass-adhesive bilayer system then behaves tridimensionally. On the other hand, the phase-shifting coefficients exhibit a significant temperature dependence and such a fact offers a way for fine adjustment of the spacer structure. With this aim, the nonlinear mirror was placed on a thermoelectric cooler device providing a range of background temperatures.

The cavity mirrors were a nickel-chrome (80:20) film of 6 nm thickness coated on the first layer of glass and a TiO_2-SiO_2 multilayer stack coated either on the rear glass layer, in the trilayer structure, or on a 1-mm glass substrate external to the cavity, in the bilayer system. The dielectric mirror reflection was high (>0.98 for the operating wavelength) while the metallic mirror had external and internal reflections of 0.17 and 0.23, respectively, and transmission of 0.46. The cavity finesse was really low, but it must be stressed that cavities with absorbing input mirrors behave very differently from the usual lossless case. Contrast and finesse may be independent in cavities with input mirror absorption and high contrast may be achieved if the transmission and reflection phase shifts of the absorbing film are such that the transmission and reflection of the interferometer present in-phase intensities [21]. In our devices the output intensities behave with a relative phase of about 0.1π and the reflection varies from 0.07 to 0.88 while the transmission is always lower than 0.005.

The device was irradiated with a continuous-wave laser beam of 488-nm wavelength focused to a 0.3-mm-diam spot, the reflected light was detected by means of a photodiode, and the signal was digitized and stored in a computer. The light beam was provided by an argon-ion laser and power fluctuations of the output beam were reduced to less than 0.1% by means of an electro-optic modulator subjected to an optical feedback loop. The stabilized beam was circularly polarized with a $\lambda/4$ plate. The light polarization had no role in the experiment because the nonlinear device contained isotropic materials only and the light beam incidence was almost normal. Nevertheless, the $\lambda/4$ plate, jointly with the output polarizer of the modulator, worked as an optical isolator avoiding any return of light to the laser cavity and the consequent instabilities.

V. RESULTS AND DISCUSSION

We report here some significant results illustrating homoclinic bifurcations associated with a variety of saddle in-

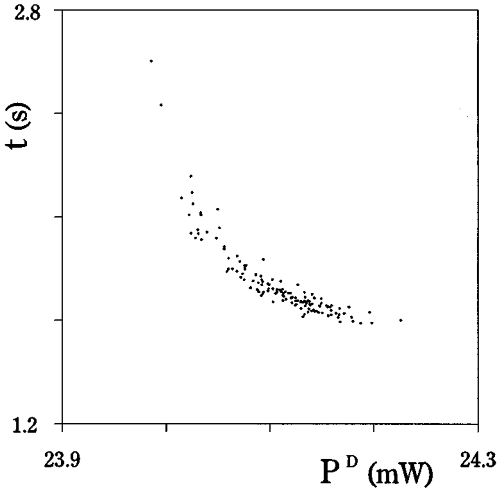

FIG. 5. Return time versus position for the points of the Poincaré section denoted D in Fig. 4.

variant sets. Figure 2 presents time evolutions of the reflected light power P for different values of the incident power and for the case of the glass-silicone-glass trilayer. The interferometric origin of the signal is responsible for some details that have to be taken into account in order to understand the observed wave forms fully. In effect, at light powers such that nonlinear effects sustain phase-shift variations larger than 2π, the reflected power varies between its maximum and minimum values with a sudden folding at these points. Such folds are absent in the time evolution of the phase shift ψ and they have no dynamical significance.

Figure 2 shows also projected phase portraits obtained from the time signals by an embedding technique. The representations have been done in the three-dimensional space defined by $P(t)$, $P(t+\tau)$, and $P(t+2\tau)$, with τ almost equal to one-quarter of the small oscillation period ($\tau=90$ ms in the case of Fig. 2). The reported phase portraits usually represent five complete orbits, even if the recorded time signals contain always more than 100 long period oscillations. Notice the influence of the $P(t)$ interferometric folding in the reconstructed phase portraits.

The presence of an inward spiraling focus, at which the orbit gradually approaches, is clear from both the time evolutions and phase portraits of Fig. 2. The number of high-frequency oscillations and the period of the low-frequency oscillation increase up to the homoclinic transition at 49.8 mW, in which the orbit is destroyed and the system goes to a different oscillating state associated with another stationary solution of the multistable branching diagram. The signals always appear to be periodic. In effect, for the signal closer to homoclinicity (49.2 mW), the greatest Lyapunov exponent calculated with the algorithm of Ref. [29] is $-0.21T^{-1}$, where $T=0.36$ s denotes the period of the small oscillations. On the other hand, by assuming a linear motion around the saddle governed by eigenvalues λ and $\rho\pm i\omega$, we obtained $\omega=17.2$ s^{-1} and $\rho=-2.4$ s^{-1} from the time signal, and $\lambda=0.01$ s^{-1} from a projection of the phase-space flow over a direction close to the unstable saddle dimension. It is clear that such eigenvalues do not fulfill the Shil'nikov condition $|\rho/\lambda|<1$.

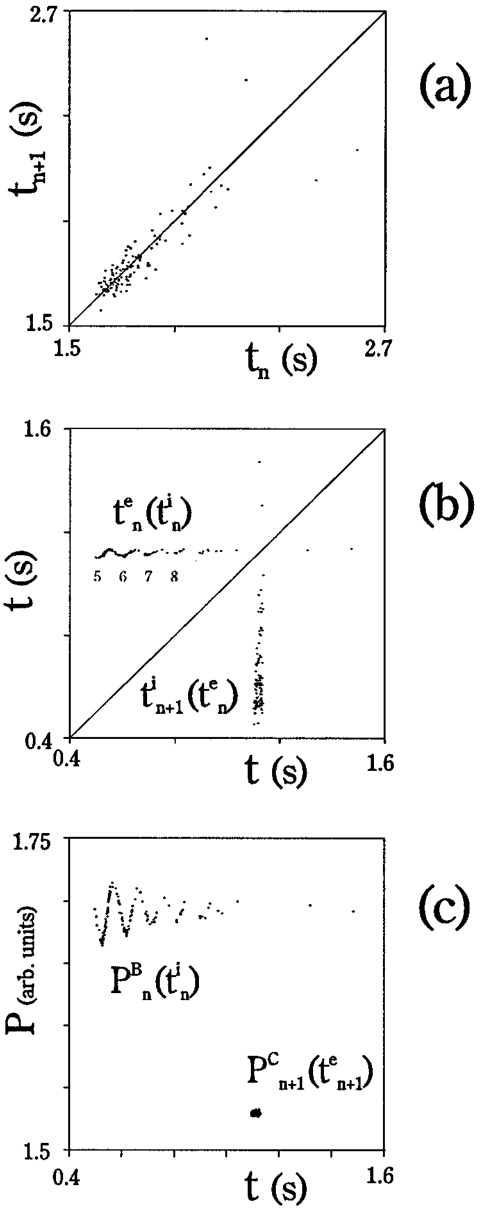

FIG. 6. Return map representations for the 37.2-mW signal: (a) first-return time map for section C, (b) two-stage time return map between sections B and C, and (c) space coordinate versus flying time for the two-stage map. Numeric symbols in (b) indicate the number of high-frequency oscillations in the corresponding orbits.

A different situation may be seen in Fig. 3, where we present results obtained with the glass-adhesive bilayer system and for a thermoelectric cooler temperature of 25 °C. Phase portraits have been reconstructed with an embedding delay of 30 ms. The saddle eigenvalues estimated form the case closer to homoclinicity (37.2 mW) have been found equal to 4.4 and $-3.7\pm i66.1$ s^{-1}. Such eigenvalues verify the Shil'nikov condition very closely, suggesting that chaos could appear very near homoclinicity only. The aperiodic signal at 37.2 mW contains orbits including 5–14 high-frequency oscillations and the corresponding greatest Lyapunov coefficient has been found to be $+0.12T^{-1}$, with $T=95$ ms denoting the period of high-frequency oscillations. Details of the attractor structure may be appreciated in the

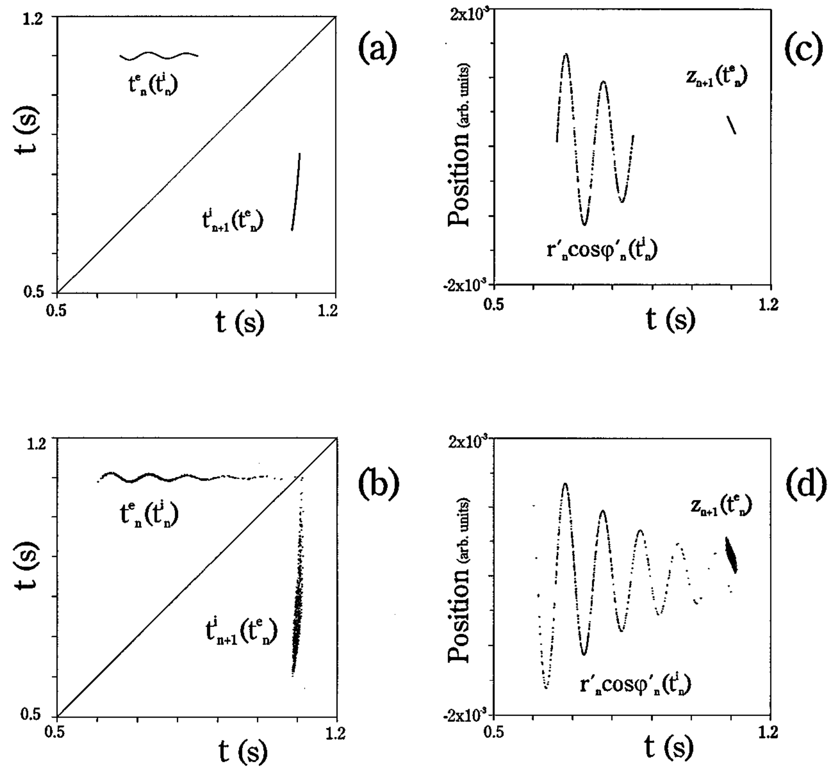

FIG. 7. Two-stage time return map (a) represented from the Poincaré map model and (b) the same with random noise introduced on the phase-space variables at each map step. Positions on the two Poincaré map sections versus the previous flying time between such sections, (c) without noise and (d) with noise.

Poincaré sections shown in Fig. 4, where each section contains 138 intersection points. The sections correspond to differently oriented planes and have been correspondingly enlarged. The scales in mW indicate the metric length associated with each represented plane. Section A corresponds to a section within the conical screw, close to the saddle focus, and normal to the unstable manifold. Section B is located at the end of the screw, normal also to the unstable saddle manifold, and the representation is enlarged 20 times with respect to A. Sections C and D have been taken normal to the flow. The attractor section area is minimum in C and we consider this point as the end of the nonlinear reinjection initiated at B and the beginning of the saddle influence region. The spiral structure clearly seen in section A confirms the presence of a saddle-focus singularity governing the flow in this phase-space region and, according to the Poincaré map model, its well defined shape indicates that the reinjection flow reaches the saddle influence region with a narrow line section almost parallel to the unstable manifold, i.e., with a well definite φ_n value. In effect, eliminating the time in Eqs. (1), one obtains the parametric relation

$$r'_n(\varphi'_n)=\exp\left[\frac{\rho}{\omega}(\varphi'_n-\varphi_n)\right] \tag{7}$$

that applies for any z constant plane within the linear region. By assuming a fixed φ_n value, the representation of Eq. (7) for a given range of φ'_n values describe a segment of spiral centered on the z axis, i.e., on the unstable manifold. The radius attenuation per spiraling turn provides a direct estimate for ρ/ω in agreement with the values obtained from the time signal. The length of the spiral and its approach to the center indicate how close the system is to homoclinicity. Furthermore, by proper numbering of intersection points we have verified that the spiral points appear almost ordered according to the previous longitudinal position on section D, i.e., the spiral points in A move away from the center according to the distance to one of the attractor ends in section D. It then seems clear that the saddle stable manifold is very close to this end of the attractor section D. Complementary information is provided by Fig. 5, where the return time from D to D is represented versus the coordinate $P(t)$ of the departure points. The time asymptotic divergence confirms how close to homoclinicity the system is.

From section A to C the flow section strongly contracts with a slight asymmetry denoting stronger contraction in a given direction. The spiral structure vanishes along the flow under the combined action of contraction and noise and we estimate the transverse size of section C as essentially due to noise. From C to D the attractor section exhibits one-dimensional expansion (stretching) that may be associated with saddle repulsion because the repulsion rate enhances with the distance to the saddle attracting manifold.

The flow contraction points out that BOITAL systems are strongly dissipative and the more pronounced contraction along a given direction suggests one-dimensional Poincaré sections and the consequent possibility of 1D return maps. Nevertheless, Fig. 6(a) presents a first-return map obtained for Poincaré section C by representing the return time of an orbit as a function of the return time of the previous orbit and the absence of any structure suggests that noise is strong enough to interrupt deterministic correlations between successive orbits at high degree. Thus, even if a really low noise level is apparent in the time evolution signals, the strong flow contraction makes its influence especially crucial where

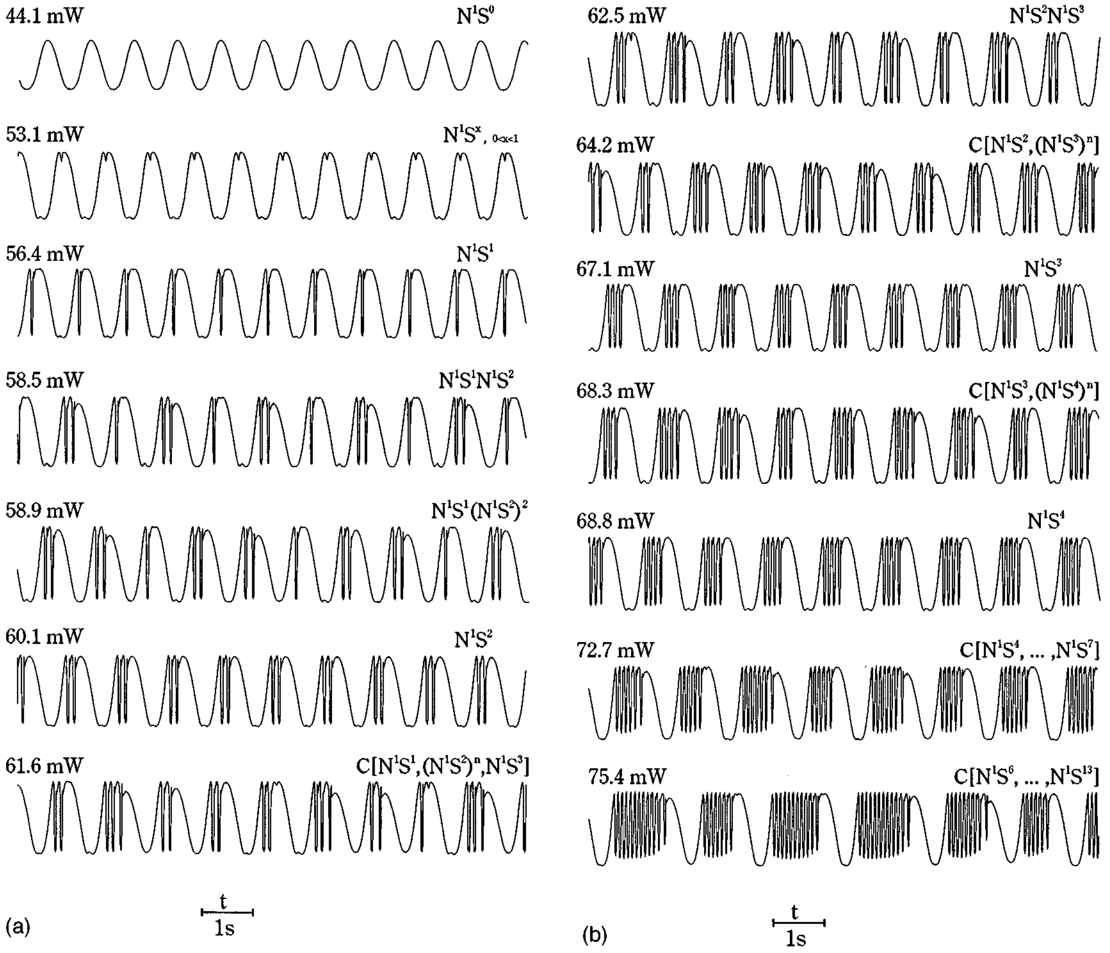

FIG. 8. Time evolution of reflected power for different incident powers and for the same device as in Fig. 3, but at 18°C.

the attractor section seems dominated by noise, i.e., in section *C* of Fig. 4. The localization of noise effects upon the attractor is pointed out by the two-stage time return map of Fig. 6(b). In this representation t_n^i is the internal time spent by a given orbit around the saddle, from sections *C* to *B*, and t_n^e is the reinjection time from *B* to *C* for the same orbit. Notice that intersection with the bisectrix have no significance in this two stage return representation. The well-defined structure of $t_n^e(t_n^i)$ indicates that the inner motion determines the following reinjection time with a very limited influence of noise, while the broad appearance of $t_{n+1}^i(t_n^e)$ reflects a strong noise influence on the next internal time as a function of previous external time. Each hump appearing on $t_n^e(t_n^i)$ corresponds to orbits containing a given number of high-frequency oscillations and then a numeric symbol may be associated with it.

The two-stage time return map is reproduced very well by the Poincaré map model, as shown in Fig. 7. Figure 7(a) represents Eqs. (6) with $\rho=-3.7$, $\omega=66.1$, $\lambda=4.4$, $b=3\times10^{-4}$, $\beta=65$, $f=0.12$, $\gamma=\pi$, and $T^e=1.1$. A constant equal to -1.1 has been added to the internal time given by Eq. (6b) to compensate for differences in Poincaré section positions on the theoretical and experimental phase portraits. Figure 7(b) shows the influence of a random noise introduced on the phase-space variables z_n, φ_n, r_n', and φ_n' at each recurrent step of the map calculation, with maximum amplitudes of 1.2×10^{-4}, 0.3, 3×10^{-4}, and 0.3, respectively. Figure 7(c) shows that the ranges of z_n and r_n' values cover intervals of about 5×10^{-4} and 1.5×10^{-3}, respectively, and it may be then realized that the noise amplitude introduced represents 20% of such intervals.

Similar but complementary information is obtained from the experimental map of Fig. 6(c), where the coordinate $P(t)$ of points of either section *B* or section *C* is represented as a function of the previous flying time from *C* to *B* or from *B* to *C*, respectively. The coordinate $P(t)$ is close to the long

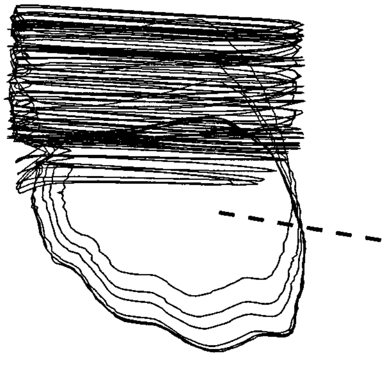

FIG. 9. Reconstructed phase portrait from the 75.4-mW signal of Fig. 8.

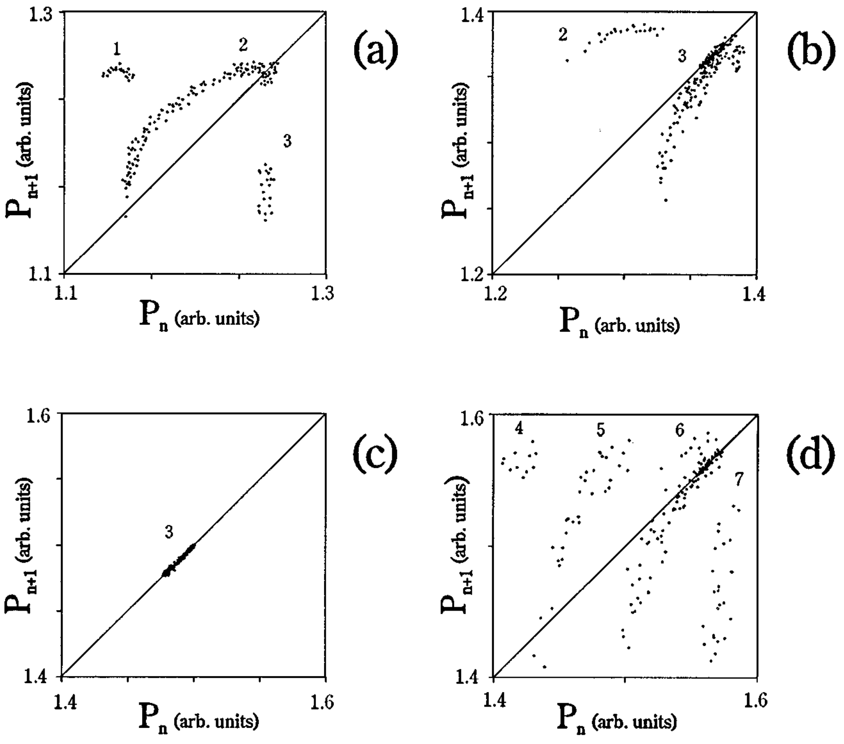

FIG. 10. First-return maps representing the phase-space coordinate $P(t)$ for various signals of Fig. 8. Input powers are (a) 61.6 mW, (b) 64.2 mW, (c) 67.1 mW, and (d) 72.7 mW. Numeric symbols indicate the number of high-frequency oscillations contained in the orbit.

dimension of the attractor section B and gives maps with the best defined structure. On the basis of the Poincaré map model, the representations of Fig. 6(c) may be associated with the equations

$$r_n'\cos\varphi_n' = \exp(\rho t_n^i)\cos\{\omega t_n^i - [\exp(-\lambda t_n^i) - b]\tan\gamma\}, \tag{8a}$$

$$z_{n+1} = b - \frac{t_n^e - T^e}{\beta}, \tag{8b}$$

which have been represented in Figs. 7(c) and 7(d), without and with the addition of noise, respectively. The relative vertical positions of the two map structures have no significance when compared to the experimental representation of Fig. 6(c). It is seen that, according to the experiment, the noise exerts a strong influence on $z_{n+1}(t_n^e)$, but not on the shape of $r_n'\cos\varphi_n'(t_n^i)$. Thus we infer that the longitudinal position on section B is well determined as a function of the previous flying internal time, without a significant influence of noise, while any deterministic correlation between the reinjection position on C and the previous reinjection time seems lost.

A low level of noise may cause strong consequences for just the same reason that chaotic dynamics may arise from the extreme sensitivity of the flow when it reinjects towards the saddle point close to homoclinicity. A bit of noise on the reinjection coordinate z_n causes hesitation between orbits with a different number of high-frequency oscillations and the consequent enlargement of the internal time range. Nevertheless, the internal time t_n^i and the corresponding outgoing position from the saddle influence region $r_n'\cos\varphi_n'$ remain very well correlated [Fig. 7(d)]. In the reinjection step, the relative influence of noise is more pronounced on the reinjection coordinate z_{n+1} than on the external time t_n^e. Thus t_n^e even maintains a good correlation with t_n^i [Fig. 7(b)], while $z_{n+1}(t_n^e)$ presents significant vertical broadening [Fig. 7(d)]. This z broadening is of the order of both the range of z values and the homoclinicity parameter b and its consequences on the next orbit evolution may be strong enough to alter the deterministic evolution.

We have also investigated the two stage map representations of Fig. 7 in numerical time evolutions obtained by integration of the BOITAL PDE system [22]. In this case, noise has been introduced in the form of input power fluctuations with 5% maximum amplitude and randomly added at each time step of the PDE integration process. We do not present these results here because they are very similar to those of Fig. 7.

Consider now the case of Fig. 8, where we report a series of time evolutions obtained from the same glass-adhesive bilayer system as in Fig. 3 but with the thermoelectric cooler plate at 18 °C. The most relevant difference with respect to signals of Fig. 3 is the almost uniform amplitude of the high-frequency oscillations. It suggests the presence of a saddle limit cycle instead of a saddle focus. The reconstructed phase portrait shown in Fig. 9 for the 75.4-mW signal confirms that a relatively large limit cycle has been generated through a Hopf bifurcation of the saddle point. The cylindrical screw moving away from the saddle cycle turns very close to one of its unstable manifold branches, showing that such a cycle has to positive characteristic multipliers. The embedding of Fig. 9 has been done in the phase space defined by $P(t)$, $\langle P(t+\tau)\rangle_{2\tau}$, and $\langle P(t)\rangle_{20\tau}$, with $\tau = 30$ ms and the angular denoting time averages. Chaos is now observed without the requirement of being extremely close to homoclinicity and, in fact, the time dynamics as a function of the incident light power evolves as follows. There is a range of periodic oscillations with a successively increasing number of high-frequency oscillations. At a certain moment the signal becomes aperiodic (61.6 mW) and then is followed by the alternate sequence of periodic and aperiodic signals that ends with the homoclinic transition to another oscillating state (not shown in the figure). Aperiodic evolutions consist of successive long-period oscillations containing different numbers of high-frequency peaks: one, two, and three peaks (61.6 mW); two and three peaks (64.2 mW); three and four peaks (68.3 mW), four to seven peaks (72.7 mW); and six to thirteen peaks (75.4 mW). The alternate sequence of periodic and aperiodic regimes is a significant feature of homoclinic chaos.

Using a symbolic notation, we can characterize the different kinds of orbit structures by sequences of symbols such as $N^m S^n$, where m and n denote the number of consecutive low-frequency and high-frequency oscillations, respectively. N indicates the node fixed point from which the low-frequency limit cycle originated and S indicates the saddle limit cycle associated with high-frequency oscillations. Aperiodic wave forms are denoted by $C[,]$ and their structure is based on combinations of the sequence segments enclosed in the square brackets. At the beginning, we were able to appreciate a gradual transition from one orbit structure to the next one, as may be seen in the 53.1-mW signal for the $N^1S^0 \rightarrow N^1S^1$ transition, but the transitions become immediately abrupt without stable wave forms in between. According to the Poincaré map model [4,7,8], close enough to homoclinicity, each periodic window appears and disappears through a cyclic tangent bifurcation and a period-doubling sequence, respectively. Nevertheless, the control parameter noise prevents detailed observation of such bifurcations and we have only appreciated intermittent evolutions just before the periodic window appearance. This is the case of the 64.2-mW signal that may be related to the saddle-node bifurcation leading to the three-peaks periodic window (67.1 mW). Another example is given by the 68.3-mW signal, where the accumulation of successive N^1S^4 oscillations denotes the proximity to the corresponding periodic window (68.8 mW).

A deterministic correlation between successive orbits is now clearly evidenced in first-return maps. For instance, the return maps of Fig. 10 represent the coordinate $P(t)$ of intersection points in a given Poincaré section of the phase portraits derived from various signals of Fig. 8. The Poincaré section cuts the reinjection loop as indicated by a broken line on the attractor shown in Fig. 9. Each map branch corresponds again to orbits with a given number of high-frequency oscillations and the symbols indicated on the return map representations describe such numbers. The case of Fig. 10(b) corresponds to the 64.2-mW signal observed just before the appearance of the periodic oscillation with three high-frequency peaks. The form of the map points out clearly the occurrence of a type-I intermittency associated with the tangent bifurcation that will occur when the bisectrix reaches the branch with symbol 3 and the corresponding periodic orbit then appears [Fig. 10(c)]. Multiple-branched structures appear even more clearly in time return maps like the ones shown in Fig. 11. The time map of Fig. 11(a) corresponds to the same signal as the space coordinate map of Fig. 10(d), while Fig. 11(b) corresponds to the 75.4-mW signal with orbits containing 6–13 high-frequency peaks.

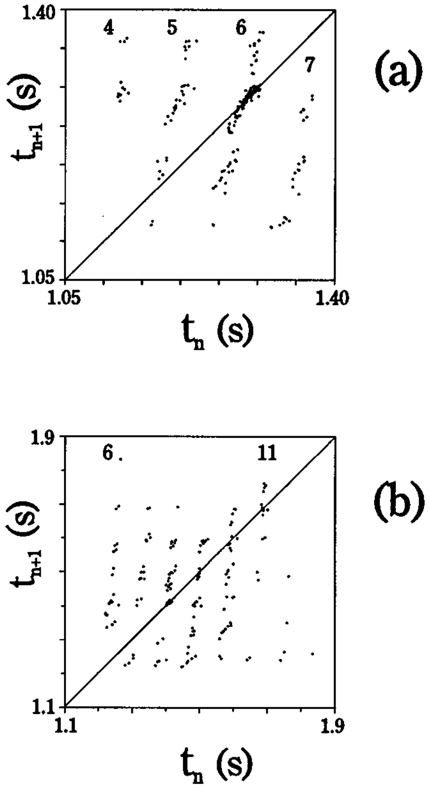

FIG. 11. First-return time return maps for two cases of Fig. 8, showing multiple branches: (a) 72.7 mW and (b) 75.4 mW.

In conclusion, a variety of nonlinear dynamical phenomena have been observed in the response of an optothermal bistable device irradiated by a laser beam and the homoclinic nature of such phenomena has been pointed out. Variation of some device parameters has allowed us to obtain homoclinic dynamics associated with saddle focus not fulfilling the Shil'nikov condition, with saddle focus fulfilling that condition and with saddle limit cycles. Clear Shil'nikov-type phase portraits have been reconstructed from time signals. In the case of a saddle focus close to the Shil'nikov condition, the attractor structure has been analyzed on proper Poincaré sections and the phase-space operations underlying the homoclinic dynamics have been evidenced. Two-stage return map representations have been used to point out the localization of noise effects on a given part of the phase portrait, i.e., where the reinjection flow reaches the saddle influence region, and to verify the internal correlation of orbits even in the case that noise is able to interrupt deterministic evolution between successive orbits. Homoclinic chaos has been clearly pointed out in the case of a saddle limit cycle. for which multiple-branched first-return maps have been obtained from the corresponding time signals.

ACKNOWLEDGMENTS

This work has been supported by the Dirección General de Investigación Científica y Técnica, under the Project No. PB93-0842.

[1] J. Gukenheimer and P. Holmes, *Nonlinear Oscillations, Dynamical Systems, and Bifurcations of Vector Fields* (Springer-Verlag, New York, 1983).

[2] J. Palis, F. Takens, *Hyperbolicity and Sensitive Chaotic Dynamics at Homoclinic Bifurcations* (Cambridge University Press, Cambridge, 1993).

[3] A. Arnéodo, P. Coullet, and C. Tresser, J. Stat. Phys. **27**, 171 (1982).

[4] P. Gaspard, R. Kapral, and G. Nicolis, J. Stat. Phys. **35**, 697 (1984).

[5] L. P. Shil'nikov, Math. USSR Sb. **6**, 443 (1963).

[6] N. K. Gavrilov and L. P. Shil'nikov, Math. USSR Sb. **17**, 467 (1972); **18**, 139 (1973).

[7] A. Arnéodo, P. Coullett, E. A. Spiegel, and C. Tresser, Physica D **14**, 327 (1985).

[8] P. Glendinning and C. Sparrow, J. Stat. Phys. **35**, 645 (1984).

[9] M. Bosch and C. Simó, Physica D **62**, 217 (1993).

[10] P. Hirschberg and E. Knobloch, Physica D **62**, 202 (1993).

[11] F. Argoul, A. Arnéodo, and P. Richetti, J. Chi, Phys. **84**, 1367 (1987).

[12] F. T. Arecchi, W. Gadomski, A. Lapucci, H. Mancini, R. Meucci, and J. A. Roversi, J. Opt. Soc. Am. B **5**, 1153 (1988).

[13] D. Hennequin, F. de Tomasi, B. Zambon, and E. Arimondo, Phys. Rev. A **37**, 2243 (1988).

[14] M. Lefranc, D. Hennequin, and D. Dangoisse, J. Opt. Soc. Am. **8**, 239 (1991).

[15] F. Papoff, A. Fioretti, and E. Arimondo, Phys. Rev. A **44**, 4639 (1991).

[16] T. Braun, J. A. Lisboa, and J. A. C. Gallas, Phys. Rev. Lett. **68**, 2770 (1992).

[17] R. Herrero, F. Boixader, G. Orriols, J. I. Rosell, and F. Pi, Opt. Commun. **113**, 324 (1994).

[18] J. J. Healey, D. S. Broomhead, K. A. Cliffe, R. Jones, and T. Mullin, Physica D **48**, 322 (1991).

[19] H. Herzael, P. Plath, and P. Svensson, Physica D **48**, 340 (1991).

[20] M. R. Basset and J. L. Hudson, J. Phys. Chem. **92**, 6963 (1988).

[21] G. Orriols, C. Schmidt-Iglesias, and F. Pi, Opt. Commun. **63**, 66 (1987).

[22] J. I. Rosell, J. Farjas, R. Herrero, F. Pi, and G. Orriols, Physica D **85**, 509 (1995).

[23] J. Farjas, J. I. Rosell, R. Herrero, R. Pons, F. Pi, and G. Orriols, Physica D (to be published).

[24] H. J. Kong and W. Y. Hwang, J. Appl. Phys. **67**, 6066 (1990).

[25] J. I. Rosell, F. Pi, F. Boixader, R. Herrero, J. Farjas, and G. Orriols, Opt. Commun. **82**, 162 (1991).

[26] O. E. Rössler, Ann. N. Y. Acad. Sci. **316**, 376 (1979).

[27] F600, Bayer AG.

[28] NOA61, Norland Products Inc.

[29] W. Briggs, Phys. Lett. A **151**, 27 (1990).